Progress In Electromagnetics Research C, Vol. 161, 239–245, 2025

PIER C

(Received 31 August 2025, Accepted 31 October 2025, Scheduled 12 November 2025)

Sub-6 GHz Dual-Polarized Dual-Mode OAM Antenna

Abdulkadir Uzun* and İbrahim Tekin

Electronics Engineering, Sabanci University, 34956 Tuzla, Istanbul, Turkey

ABSTRACT: In this paper, we present a dual-mode, dual-polarized orbital angular momentum (OAM) antenna, implemented as a four-element uniform circular array (UCA) with a series-fed network on a single-layer substrate. The novelty of the antenna lies in its ability to generate four orthogonal states simultaneously in a single transmission channel — two from $l = \pm 1$ OAM states and two from vertical/horizontal polarizations — without requiring multilayer feeds or complex phase-shifting networks. Full-wave simulations and experimental measurements have been used to validate the antenna's performance within the 5.85–6.1 GHz band. Far-field radiation patterns exhibit the characteristic vortex-beam profile, featuring a conical shape with a central null, while phase distributions reconstructed via FFT-based holography confirm the generation of distinct OAM modes. The antenna has four feed ports; of these, activating Ports 1 and 4 yields the highest OAM modal purity at 6 and 6.1 GHz, while Ports 2 and 3 peak in purity at 6.1 GHz. Owing to its compact, reconfigurable architecture, the designed and tested antenna is well-suited for integration into space- and power-constrained platforms such as UAVs, IoT devices, and full-duplex MIMO systems.

1. INTRODUCTION

Since the early days of analog voice transmission in the first-generation cellular networks, to the applications enabled by 5G, such as video conferencing, virtual reality, cloud computing, and smart internet of things (IoT) systems, the evolution of wireless communication has been both rapid and transformative. With the advent of 6G, there will be a demand for data rates exceeding 10 Gbps [1], along with more spectral efficiency and massive connectivity support. Addressing these challenges requires innovations at the physical layer, including a higher spectrum utilization and advanced multiplexing strategies. In this regard, orbital angular momentum (OAM) has gained recognition on a global scale for its ability to address these needs. Furthermore, the ITU-R Working Party 5D (WP 5D), responsible for terrestrial elements of International Mobile Telecommunications (IMT), has highlighted OAM as an enabling technology for IMT-2030 (6G) networks [2].

Since Thidé et al.'s 2007 work [3], OAM has attracted attention in the radio frequency (RF) domain. OAM-carrying vortex beams feature a helical phase structure described by $e^{jl\phi}$, where j is the imaginary unit, l the OAM mode number, and ϕ the azimuthal angle. Over a full 2π rotation, the phase of an OAM wave advances by $2\pi l$, leading to a helical wavefront whose number of spirals per wavelength is determined by the OAM mode number. These beams exhibit two key characteristics: orthogonality between different modes and the divergence of beams. The property of orthogonality can be utilized for multiplexing to increase the capacity and spectrum efficiency in communication systems [4], whereas the divergence property can be used in the future to replace conical scanning antennas [5, 6].

Since their original design, OAM beams have been generated using various techniques across optical, acoustic, and radio frequency (RF) domains. In RF, methods include spiral phase plates, holographic gratings, metamaterials, and especially uniform circular arrays (UCAs) [7, 8], which stand out for their compactness and phased array compatibility. However, most UCA-based designs require switches or complex feeds for mode and polarization control [6, 9–13]. The proposed antenna (Fig. 1) is more simplified in its design, enabling ±1 OAM modes in both polarizations solely by port selection.

Recent research on OAM antenna design has focused on improving mode configurability and polarization diversity, while simplifying feeding mechanisms, though often this leads to greater structural or circuit complexity. For instance, Rao et al. [9] employed three PIN diodes to switch among modes 0, $+1$, and -1 using a circularly polarized (CP) UCA and central linearly polarized (LP) elements, though the configuration produced linearly polarized OAM modes. Veerabathini et al. [10] used stacked dual-feed networks to excite rotated elliptical patches for dual-mode generation. An et al. [11] proposed a passive ring array, leveraging spatial rotation for fixed-mode generation, offering structural simplicity but limited flexibility. Naseri et al. [12] avoided diode switching by integrating varactor-based phase shifters into a low-profile UCA for tunable ±1 modes. Wu et al. [13] demonstrated a sequentially rotated feed network for wideband dual-CP OAM generation with high purity.

Unlike prior works that rely on electronic components or stacked feed networks for mode control, the antenna proposed in this work can uniquely achieve four distinct OAM states (±1 vertical and ±1 horizontal polarizations) without any electronic switches, multilayer feed networks, or phase shifters. Hence, the orthogonality of OAM modes and the orthogonal polariza-

---

* Corresponding author: Abdulkadir Uzun (kadiruzun@sabanciuniv.edu).

doi:10.2528/PIERC25083101

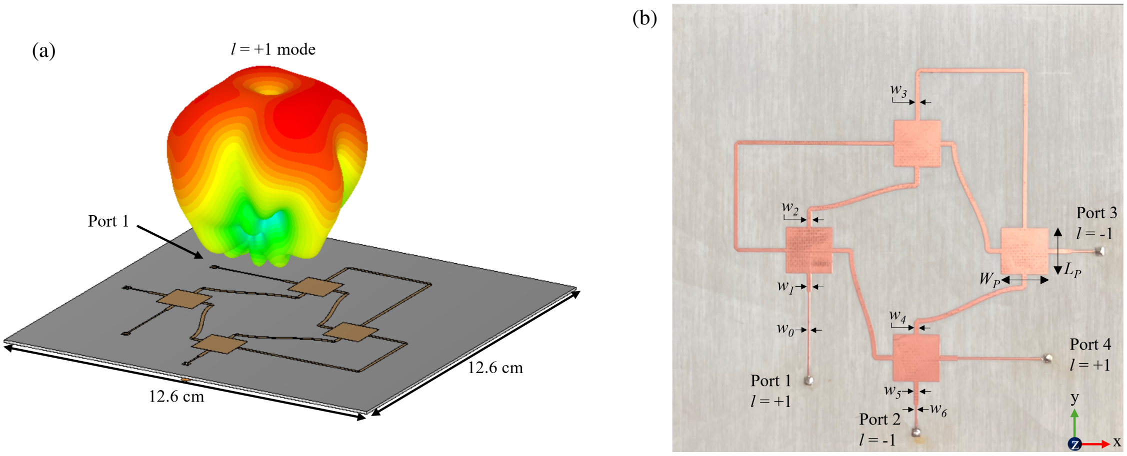

FIGURE 1. Proposed antenna. (a) Design and vortex beam of port 1 excitation. (b) Implementation.

tions of beams enable us to achieve four orthogonal states in one communication channel. The proposed antenna is a single-layer, series-fed UCA with four ports, implemented on a low-loss RO4003 substrate. Reconfigurability is achieved solely through port selection, enabling variations of both the OAM mode and polarization, without any active components or complex feed structures. This results in a highly compact, structurally simple and reconfigurable platform for dual-polarized OAM communication. This design is particularly well suited for integration into space- and power-constrained systems such as unmanned aerial vehicles (UAVs) or IoT platforms. Moreover, the orthogonal feeding scheme proposed in this work is well aligned with the full-duplex MIMO schemes [14].

2. ANTENNA DESIGN

2.1. OAM UCA Theory

An OAM-generating UCA with N microstrip elements, representatively shown in Fig. 2, is designed such that the first and last elements are fed with equal amplitude, and a total phase difference of $2\pi l$ is introduced across the array. This design ensures that each consecutive element is fed with a uniform phase increment of $\delta\varphi = 2\pi l/N$, where l is the OAM mode number.

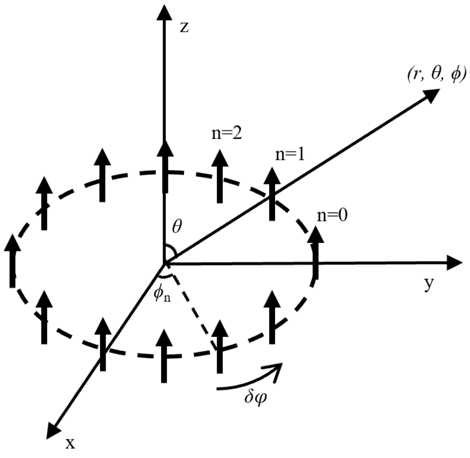

FIGURE 2. N-element OAM generating UCA.

Under this configuration, the array can generate OAM modes satisfying the condition in (1).

$$-N/2 < l < N/2 \tag{1}$$

The excitation of the nth element in the uniform circular array (UCA) to generate an OAM mode l is given in phasor form by

$$I_n = Ie^{j[\phi_0 + (n-1)\frac{2\pi l}{N}]} \quad (n = 1, 2, \dots, N) \tag{2}$$

where ϕ_0 is the initial excitation phase of the first element, l the OAM mode number, and I the excitation amplitude. The progressive phase shift between adjacent elements is denoted by $\delta\varphi = 2\pi l/N$, as illustrated in Fig. 2.

The total electric field at a far-field observation point P, due to N isotropic elements uniformly spaced on a circle of radius a, is given by

$$\vec{E}(r,\theta,\phi) = \frac{Ie^{-jkr}}{r} \sum_{n=1}^{N} e^{j[ka \sin\theta \cos(\phi - \varphi_n) + \phi_0 + (n-1)\delta\varphi]} \, \hat{a}_r \tag{3}$$

where $\varphi_n = 2\pi(n-1)/N$ is the azimuthal angle of the nth element. This formulation corresponds to the generation of an OAM mode of order l, with a total azimuthal phase variation of $2\pi l$ across the array. For instance, to generate the mode $l = \pm 1$ with $N = 4$ elements, the phase difference between adjacent elements is $\Delta\phi = \pm 90°$.

2.2. Proposed OAM UCA Design

In this work, we introduce a compact, single-layer feeding structure capable of generating dual-mode, dual-polarized OAM beams with a four-element UCA, as illustrated in Fig. 1. A series-fed network along both the x- and y-axes ensures equal power division and precise phase progression for $l = \pm 1$ modes. The UCA radius is optimized to 29 mm, enabling accurate inter-element spacing and required phase shifts. To compensate for the 180° polarization reversal between the second and third patches, the interconnect line is lengthened to add a 180° phase shift, yielding a total 270° phase difference.

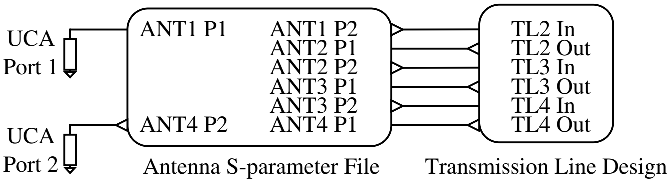

FIGURE 3. Co-design framework of the series-fed UCA. Each patch element is modeled with two ports (e.g., ANT1 P1: port 1 of patch 1, ANT1 P2: port 2 patch 1), resulting in an eight-port representation of the four-patch array. The transmission line sections (e.g., TL2: interconnect between patch 1 and patch 2, TL3: interconnect between patch 2 and patch 3, TL4: interconnect between patch 3 and patch 4) connect adjacent antenna elements in series. Ports 1 and 2 indicate the symmetric excitation points located at the opposite ends of the array.

The feeding network was initially designed for a single linear polarization and subsequently reused for dual-polarized operation by rotating the structure by 90°. To ensure proper performance in both polarizations, a final joint optimization of the complete four-port configuration was carried out at the end of the design process. This approach enabled dual-polarized OAM generation using a single compact, single-layer feed structure without the need for multilayer substrates or additional circuitry. Building on this conceptual configuration, the detailed feeding network was designed and optimized as follows. First, a single patch element with input and output ports was modeled in CST Microwave Studio. Four identical elements were then arranged in a circular configuration, forming an eight-port UCA model. The S-parameters of this model were extracted to characterize the input impedance and transmission behavior of the cascade. The schematic model was then coupled with a 3D microstrip interconnect layout in CST, as illustrated in Fig. 3. In this hybrid schematic — 3D environment, the imported antenna S-parameters (left block) were embedded together with the parametrized interconnects (right block), enabling mixed-mode co-simulation. The interconnect lines were optimized using a particle swarm optimization (PSO) routine, with the objective function defined to achieve: (i) return losses below -10 dB at both ports for the design frequency, and (ii) correct cumulative phase progression, including the necessary compensation between the second and third elements. The optimized design parameters are summarized in in Table 1.

TABLE 1. Essential geometric and electrical parameters of the antenna.

Parameter	Symbol/Ref.	Value/Notes
Patch length	L_P	12.5 mm
Patch width	W_P	12.5 mm
Substrate	-	RO4003C
Substrate thickness	h	0.813 mm
Copper thickness	t_{Cu}	35 µm
TL0, TL6 width	w_0, w_6	0.5 mm
TL1, TL5 width	w_1, w_5	1.2 mm
TL2, TL4 width	w_2, w_4	1.2 mm
TL3 width	w_3	1 mm
Reference frequency	f_0	6.0 GHz
Connector type	-	SMA end-launch, 50 Ω
Connector part number	-	Amphenol 132323

With the optimized feeding network in place, the antenna supports selectable OAM modes and polarizations through port excitation. Specifically, Ports 1 and 4 generate $l = +1$ modes, while Ports 2 and 3 generate $l = -1$. The beams from Ports 1 and 2 are y-polarized, and those from Ports 3 and 4 are x-polarized. The four-port antenna is designed and implemented on a 0.813 mm thick RO4003 substrate with dimensions of 12.6 cm × 12.6 cm.

3. ANTENNA MEASUREMENT SYSTEM

In this section, a brief description of the antenna measurement system is provided. Antenna measurements were conducted in an anechoic chamber of the Sabancı University Nanotechnology Research and Application Center (SUNUM) using a vector network analyzer and a spherical near-field antenna measurement system. The setup incorporates automated positioners that enable independent rotation in both azimuth (ϕ) and elevation (θ) directions, as illustrated in Fig. 4. The antenna under test placed in the anechoic chamber is shown in Fig. 5.

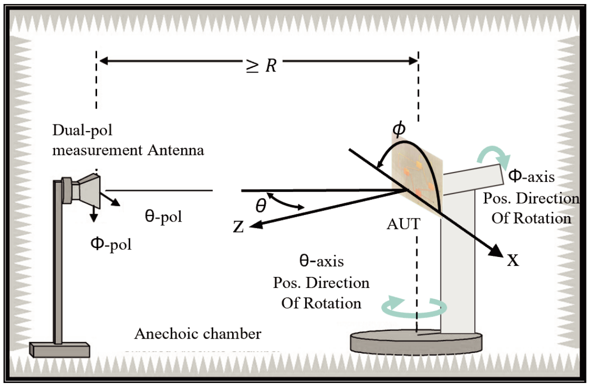

FIGURE 4. Schematic representation of the anechoic chamber measurement setup and axis definitions for antenna characterization [15].

4. RESULTS AND DISCUSSION

This section presents the results of the antenna simulations and measurements. The designed antenna was analyzed in Computer Simulation Technology (CST) Studio Suite 2022 using the frequency-domain solver. For experimental validation, the dual-mode OAM antenna was measured to obtain its S-parameters, realized far-field gain pattern, and phase distribution. In Fig. 6, the simulated and measured port reflection coefficients are presented.

To assess the polarization performance and verify OAM mode generation across the operating band, the radiation patterns measured for each port are analyzed below. The radiation pattern measurements were conducted sequentially for horizontal (y-polarized) and vertical (x-polarized) polarizations, and the full 2D results for $l = +1$ for both x- and y-polarizations are presented in Figs. 7 and 8. Each figure shows six subplots, covering both polarizations at 5.9, 5.95, and 6.0 GHz. The valley

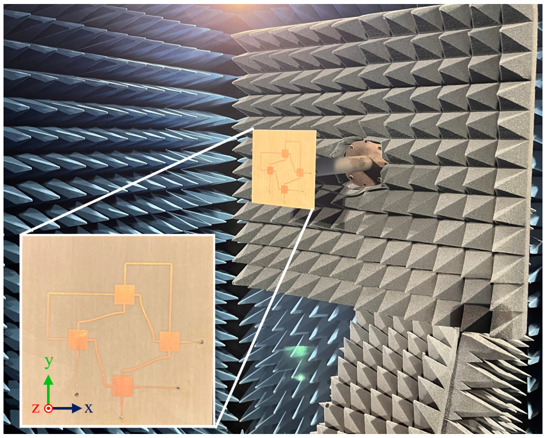

FIGURE 5. Measurement setup in the anechoic chamber, showing the dual-mode OAM antenna under test (inset: fabricated antenna).

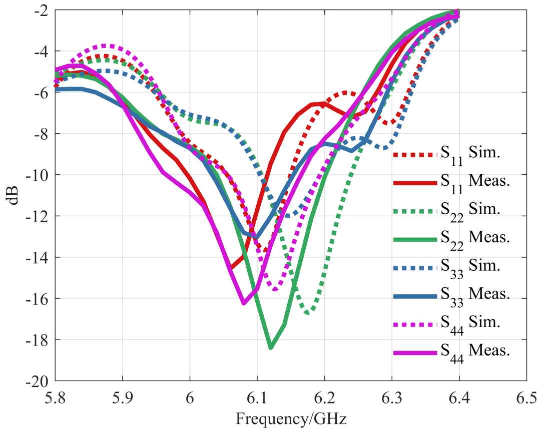

FIGURE 6. Measured and simulated port reflection coefficients.

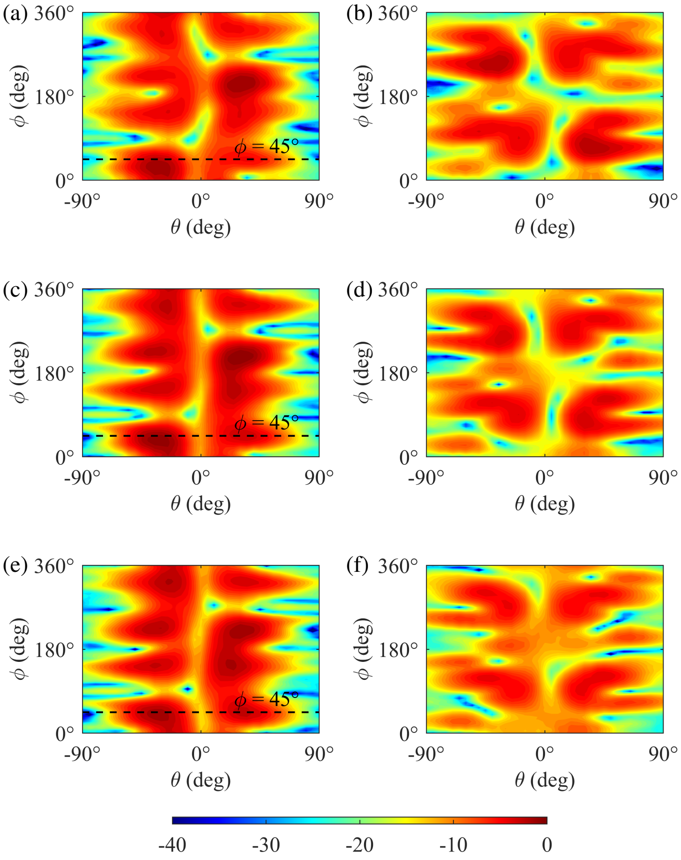

FIGURE 7. Equirectangular projection of measured Port 1 patterns. Left column: y-pol (co-pol). Right column: x-pol (cross-pol). Rows correspond to (a), (b) 5.9 GHz, (c), (d) 5.95 GHz, and (e), (f) 6.0 GHz.

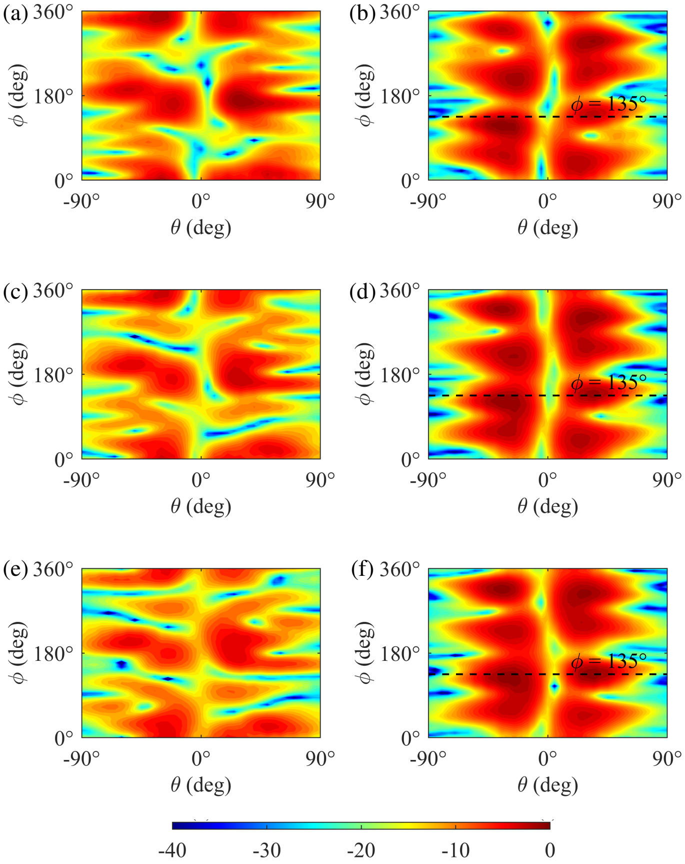

FIGURE 8. Equirectangular projection of measured Port 4 patterns. Left column: y-pol (cross-pol). Right column: x-pol (co-pol). Rows correspond to (a), (b) 5.9 GHz, (c), (d) 5.95 GHz, and (e), (f) 6.0 GHz.

alongside $\theta = 0°$ in the equirectangular projection of the measured patterns corresponds to the null at the beam center. When the locations of peak gain values are analyzed in these plots, they clearly reveal the principal radiation directions. Consequently, radiation cuts were also taken at $\phi = 45°$ for Ports 1 and 2, and at $\phi = 135°$ for Ports 3 and 4, which are not E- and H-planes of the antenna, but rather in the region between these planes. For comparison with the simulated realized gain, the total measured gain was computed by coherently summing the power contributions of both polarizations as below.

$$G_{\text{meas}} = 10 \log_{10} \left(10^{G_x/10} + 10^{G_y/10} \right) \tag{4}$$

The combined measurement is shown alongside the simulated gain in Fig. 9. The radiation cuts are taken at $\phi = 45^\circ$ for Ports 1 and 2, and at $\phi = 135^\circ$ for Ports 3 and 4. These selections are appropriate, as the two port groups are orthogonally oriented with respect to each other.

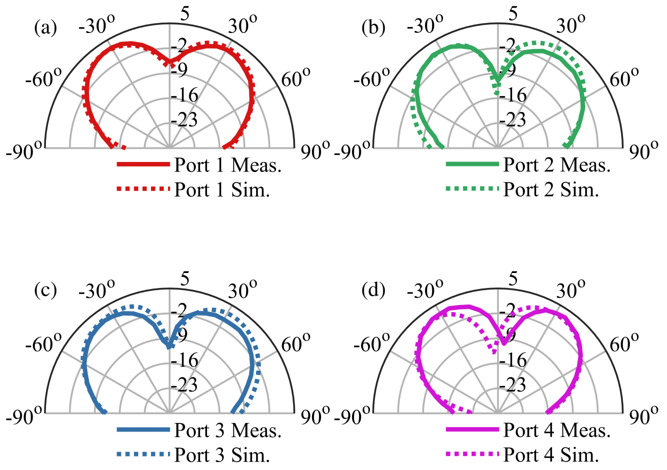

FIGURE 9. Measured and simulated realized gain patterns. (a) Port 1 excitation. (b) Port 2 excitation. (c) Port 3 excitation. (d) Port 4 excitation.

Furthermore, Fig. 10 depicts the peak values of the measured realized gain across the 5.8–6.25 GHz frequency range for all four ports. The peak realized gain values are extracted along azimuthal planes of $\phi = 45^\circ$ for Ports 1 and 2, and $\phi = 135^\circ$ for Ports 3 and 4. These planes are determined as the dominant directions of the OAM radiation. A dip in gain is observed between 5.85 GHz and 6.1 GHz, corresponding to the frequency range where the OAM mode is most effectively generated. In this frequency range, the antenna produces a doughnut-shaped beam with a divergence angle of approximately 30° (See Fig. 9), resulting in a lower peak gain due to the reduced directivity. The observed increase in gain beyond 6.15 GHz indicates a transition toward a more directive radiation pattern, where the antenna behavior deviates from vortex-mode characteristics and begins to concentrate energy closer to the boresight.

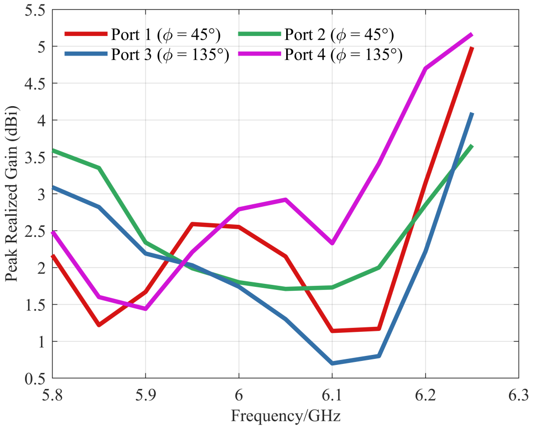

FIGURE 10. Measured realized gain versus frequency for each port of the proposed antenna. The peak realized gains are 2.55 dBi (Port 1), 1.80 dBi (Port 2), 1.75 dBi (Port 3), and 2.79 dBi (Port 4).

Finally, the phase distributions were obtained 30 cm away from the antenna, using the fast Fourier transform (FFT) hologram reconstruction algorithm provided in NSI2000 software, with an FFT size of 1024×128. The spatial extent of the reconstructed field distribution spans 0.3048 m along both the x- and y-axes. The results are presented in Fig. 11 for Ports 1 through 4. Since Port 1 and Port 2 are primarily y-polarized, only the E_y phase distributions are shown for these ports. Conversely, as Port 3 and Port 4 are x-polarized, only the E_x phase distributions are provided. For each port, distributions are given at 6.0 GHz and 6.1 GHz to illustrate frequency dependence. The phase contours indicate purer OAM behavior for Ports 1 and 4 at 6.0 GHz, while Ports 2 and 3 exhibit clearer mode formation at 6.1 GHz.

To quantify these observations, simulated OAM mode purities were computed at the same observation plane ($z = 300$ mm) on circular sampling contours of $r = 90$ mm and $r = 120$ mm. Table 2 summarizes the simulated purities for Ports 1 and 4 at 6.0 GHz and 6.1 GHz. Consistent with the phase contours, Ports 1 and 4 attain higher purities at 6.0 GHz, whereas Ports 2 and 3 show a marked increase at 6.1 GHz. This agreement between the measured phase distributions and simulated purity values supports the OAM performance of the proposed antenna.

TABLE 2. OAM purity evaluated at an observation plane 300 mm from the aperture and along circular contours of radius 90 mm and 120 mm.

6.0 GHz			6.1 GHz		
Port	r (mm)	Purity (%)	Port	r (mm)	Purity (%)
1	90	84.5	1	90	64.7
	120	92.9		120	78.2
2	90	76.6	2	90	69.8
	120	88.3		120	84.8
3	90	75.8	3	90	71.2
	120	88.1		120	84.5
4	90	81.3	4	90	64.1
	120	90.6		120	78.5

To contextualize the performance of the proposed antenna, Table 3 summarizes representative OAM antenna designs reported in the recent literature. The comparison highlights the diversity of element types, reconfiguration mechanisms, and structural choices employed in prior works, ranging from stacked dual-feed patches and aperture-coupled CP elements to substrate integrated waveguide (SIW)-based MIMO structures with varactor tuning. Most of these approaches rely on multilayer configurations [16, 17], active components such as PIN diodes or varactors [16, 18], or complex feeding networks [17] to achieve mode reconfigurability or polarization diversity. While such methods enable flexibility, they also increase fabrication cost, insertion loss, and structural complexity. Other studies have pursued high gain or dual-band operation [19] but typically support only a single polarization. In contrast, the proposed antenna achieves dual-mode ($l = \pm 1$) and dual-linear

TABLE 3. Comparison of the proposed antenna with representative OAM antenna designs in the literature.

Ref.	Freq. (GHz)	Polarization	l	Gain (dBi)	N	Layer	Size (mm^3)	Element Type	Reconfig. Method
[16]	2.29–2.59	HP HP VP VP	$+1$ -1 $+1$ -1	5.2	4	Three-layer	$170 \times 170 \times 7.8$	Stacked dual-feed microstrip patches	PIN diodes in feed
[17]	3.37–3.41	LHCP RHCP	$+1$ -1	3.5	8	Dual-layer	$158 \times 158 \times 3.95$	Aperture-coupled CP patches	SPDT + PIN diodes with phase-shifting dividers
[18]	3.8–4.4	$+45°$ Slant $+45°$ Slant $-45°$ Slant $-45°$ Slant	$+1$ -1 $+1$ -1	> 6	8	Single-layer	–	SIW-based MIMO elements	Varactor diodes in stubs
[19]	5.3/5.77	LHCP	$+1$	9.6/11	8	Single-layer	$150 \times 140 \times 1.6$	Dual-band LHCP slotted patches	–
Prop.	5.85–6.1	HP HP VP VP	$+1$ -1 $+1$ -1	2.79	4	Single-layer	$126 \times 126 \times 0.813$	Rectangular patches	Independent Port Excitation

HP: horizontal polarization; VP: vertical polarization; LHCP: left-hand circular polarization; RHCP: right-hand circular polarization; SIW: substrate-integrated waveguide.

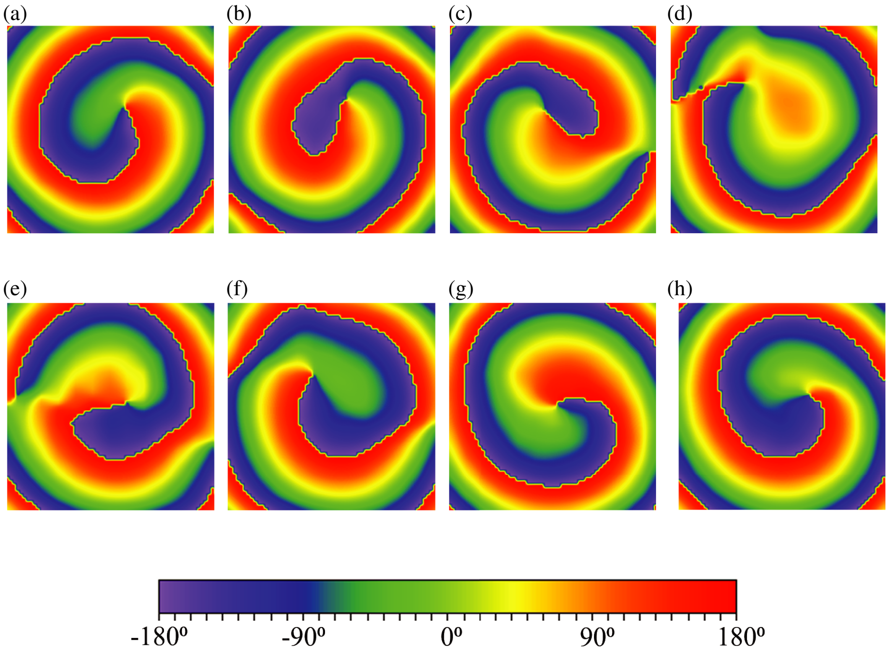

FIGURE 11. Measured phase distributions for all of the antenna ports at 6 GHz and 6.1 GHz. (a) Port 1 ($l = +1$) E_y at 6 GHz. (b) Port 1 ($l = +1$) E_y at 6.1 GHz. (c) Port 2 ($l = -1$) E_y at 6 GHz. (d) Port 2 ($l = -1$) E_y at 6.1 GHz. (e) Port 3 ($l = -1$) E_x at 6 GHz. (f) Port 3 ($l = -1$) E_x at 6.1 GHz. (g) Port 4 ($l = +1$) E_x at 6 GHz. (h) Port 4 ($l = +1$) E_x at 6.1 GHz.

polarization operation within a compact single-layer UCA, relying solely on port selection without active components, multilayer stacking, or external phase shifters. This distinction underscores the structural simplicity, fabrication economy, and integration potential of the present design compared with existing approaches.

5. CONCLUSION

As presented, this paper proposes a dual-mode, dual-polarized OAM antenna, which is a four-port, four-element UCA with a series feeding network. The novel multi-port series feeding network simplifies the structure of the antenna and allows for a single-layer RO4003 substrate to be used for easy implementation. The proposed antenna is capable of generating OAM modes of ±1 in both vertical and horizontal polarizations. The mode switching and polarization selection are done through a port selection which avoids the need for multilayer feeds or complex phase-shifting networks. The subsequent full-wave simulations and measurements suggest that the antenna can operate as an OAM antenna within the 5.85–6.1 GHz band. The vortex-beam profile and phase distributions also confirm the generation of distinct OAM modes in both orthogonal polarizations. The low-profile and small footprint architecture of the antenna allows for integration into various applications, including UAVs, IoT devices, and full-duplex MIMO systems.

ACKNOWLEDGEMENT

The authors gratefully acknowledge the support of the Nanotechnology Research and Application Center at Sabancı University for facilitating the antenna measurements in the anechoic chamber.

REFERENCES

[1] Shah, A. F. M. S., A. N. Qasim, M. A. Karabulut, H. Ilhan, and M. B. Islam, "Survey and performance evaluation of multiple access schemes for next-generation wireless communication systems," *IEEE Access*, Vol. 9, 113 428–113 442, 2021.

[2] ITU-R, "Future technology trends of terrestrial international mobile telecommunications systems towards 2030 and beyond," Report ITU–R M.2516–0, 2022, Available: https://www.itu.int/dms_pub/itu-r/opb/rep/R-REP-M.2516-2022-PDF-E.pdf.

[3] Thidé, B., H. Then, J. Sjöholm, K. Palmer, J. Bergman, T. D. Carozzi, Y. N. Istomin, N. H. Ibragimov, and R. Khamitova, "Utilization of photon orbital angular momentum in the low-frequency radio domain," *Physical Review Letters*, Vol. 99, No. 8, 087701, Aug. 2007.

[4] Drysdale, T. D., B. Allen, C. Stevens, S. J. Berry, F. C. Smith, and J. Coon, "How orbital angular momentum modes are boosting the performance of radio links," *IET Microwaves, Antennas & Propagation*, Vol. 12, No. 10, 1625–1632, 2018.

[5] Papathanasopoulos, A. and Y. Rahmat-Samii, "Fundamentals of orbital angular momentum beams: Concepts, antenna analogies, and applications," in *Electromagnetic Vortices: Wave Phenomena and Engineering Applications*, 1–32, Z. H. Jiang and D. H. Werner (eds.), IEEE Press, Wiley, 2021.

[6] Rao, M. V., Y. B. Modugu, S. Yuvaraj, and M. V. Kartikeyan, "Generation of highly azimuthal symmetric conical beam using the planar uniform circular array antenna for vehicular communication," *Applied Physics A*, Vol. 129, No. 12, 834, Nov. 2023.

[7] Chen, R., H. Zhou, M. Moretti, X. Wang, and J. Li, "Orbital angular momentum waves: Generation, detection, and emerging applications," *IEEE Communications Surveys & Tutorials*, Vol. 22, No. 2, 840–868, 2020.

[8] Noor, S. K., M. N. M. Yasin, A. M. Ismail, M. N. Osman, P. J. Soh, N. Ramli, and A. H. Rambe, "A review of orbital angular momentum vortex waves for the next generation wireless communications," *IEEE Access*, Vol. 10, 89 465–89 484, 2022.

[9] Rao, M. V., A. M. Ismail, M. N. M. Yasin, S. K. Noor, M. N. Osman, N. A. A. Rahman, J. Malik, and S. Yuvaraj, "Novel switched mode OAM beam generation using series-fed UCA antenna for AAVs," *IEEE Canadian Journal of Electrical and Computer Engineering*, Vol. 48, No. 2, 60–65, 2025.

[10] Veerabathini, S., M. V. Rao, S. Yuvaraj, and M. V. Kartikeyan, "Generation of a dual-mode OAM beam using a CP UCA antenna for wireless communication," in *2023 IEEE Wireless Antenna and Microwave Symposium (WAMS)*, 1–4, Ahmedabad, India, 2023.

[11] An, C., J. Lei, W. Li, J. Zhuo, L. Ye, and Y. Liu, "Generation of OAM beams using circular ring array with in-phase feed," *IEEE Transactions on Antennas and Propagation*, Vol. 71, No. 9, 7028–7038, 2023.

[12] Naseri, H., P. PourMohammadi, N. Melouki, A. Iqbal, and T. A. Denidni, "A low-profile antenna system for generating reconfigurable OAM-carrying beams," *IEEE Antennas and Wireless Propagation Letters*, Vol. 22, No. 2, 402–406, 2023.

[13] Wu, J., Z. Huang, X. Ren, W. E. I. Sha, and X. Wu, "Wideband millimeter-wave dual-mode dual circularly polarized OAM antenna using sequentially rotated feeding technique," *IEEE Antennas and Wireless Propagation Letters*, Vol. 19, No. 8, 1296–1300, 2020.

[14] Nawaz, H. and I. Tekin, "Dual port single patch antenna with high interport isolation for 2.4 GHz in-band full duplex wireless applications," *Microwave and Optical Technology Letters*, Vol. 58, No. 7, 1756–1759, 2016.

[15] CTIA, "Test plan for wireless device over-the-air performance: Method of measurement for radiated RF power and receiver performance," 2019, Available: https://api.ctia.org/wp-content/uploads/2019/04/CTIA_OTA_Test_Plan_3_8_2.pdf.

[16] Kang, L., H. Li, J. Zhou, and S. Zheng, "An oam-mode reconfigurable array antenna with polarization agility," *IEEE Access*, Vol. 8, 40 445–40 452, 2020.

[17] Guo, L. and Y. Chen, "Low-profile dual-layer circularly polarized orbital angular momentum uniform circular array antenna with reconfigurable OAM modes," *Journal of Electromagnetic Waves and Applications*, 1–13, 2025.

[18] Naseri, H., P. PourMohammadi, N. Melouki, F. Ahmed, A. Iqbal, and T. A. Denidni, "Reconfigurable OAM antenna with flexibility on mode numbers, polarization, and frequency," *IEEE Antennas and Wireless Propagation Letters*, Vol. 23, No. 6, 1710–1714, 2024.

[19] Rao, M. V., Y. B. Modugu, D. Mondal, S. Yuvaraj, and M. V. Kartikeyan, "Generation of dual-band OAM beam using planar uniform circular array for vehicular communications," *Microwave and Optical Technology Letters*, Vol. 66, No. 1, e13717, 2024.